

Liquid-gas-solid flows with lattice Boltzmann: Simulation of floating bodies

Simon Bogner^a, Ulrich Rüde^a

^a*Lehrstuhl für Systemsimulation, Universität Erlangen-Nürnberg, Cauerstraße 6, 91058 Erlangen*

Abstract

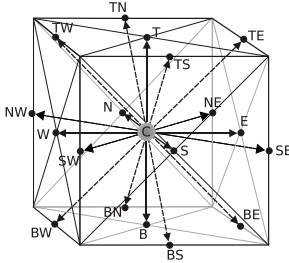
This paper presents a model for the simulation of liquid-gas-solid flows by means of the lattice Boltzmann method. The approach is built upon previous works for the simulation of liquid-solid particle suspensions on the one hand, and on a liquid-gas free surface model on the other. We show how the two approaches can be unified by a novel set of dynamic cell conversion rules. For evaluation, we concentrate on the rotational stability of non-spherical rigid bodies floating on a plane water surface – a classical hydrostatic problem known from naval architecture. We show the consistency of our method in this kind of flows and obtain convergence towards the ideal solution for the measured heeling stability of a floating box.

1. Introduction

Since its establishment the lattice Boltzmann method (LBM) has become a popular alternative in the field of complex flow simulations [33]. Its application to particle suspensions has been propelled to a significant part by the works of Ladd et al. [22, 23] and Aidun et al. [3, 4, 1]. Based on the approach of the so-called *momentum exchange method*, it is possible to calculate the hydromechanical stresses on the surface of fully resolved solid particles directly from the lattice Boltzmann boundary treatment. In this paper, the aforementioned fluid-solid coupling approach is extended to liquid-gas free surface flows, i.e., the problem of solid bodies moving freely within a flow of two immiscible fluids. We use the free surface model of [21, 30] to simulate a liquid phase in interaction with a gas by means of a *volume of fluid* approach and a special kinematic free surface boundary condition. I.e., the interface of the two phases is assumed sharp enough to be modeled by a locally defined boundary layer. This boundary layer is updated dynamically according to the liquid advection by a set of cell conversion rules.

This paper proposes a unification of the update rules of the free surface model with those of the particulate flow model, which also requires a dynamical mapping of the respective solid boundaries to the lattice Boltzmann grid. As described in [5], the resulting scheme allows full freedom of motion of the solid bodies in the flow, which can be calculated according to rigid body physics as in [20]. We demonstrate the consistency of the combined liquid-gas-solid method by means of a simple advection test with a floating body in a stratified liquid-gas channel flow, and discuss the main source of error in the dynamic boundary handling with particles in motion.

Figure 1: D3Q19 stencil. The weights are $w_0 = 1/3$ for C, $w_1, \dots, w_6 = 1/18$ for W, E, N, S, T, B, and $w_7, \dots, w_{18} = 1/36$ for TW, TE, TN, TS, NW, NE, SW, SE, BW, BE, BN, BS.



We further apply our method to the problem of rotational stability of rigid floating structures. This kind of hydromechanical problems typically emerge in marine engineering, where the floating stability of offshore structures is of concern [19, 12], such as the stability of a ship in a heeled position. Because of the static nature of the addressed problems, numerical issues arising from hydro-dynamic effects can be widely discarded, which makes them well-suited for the verification of the involved force calculations. In addition to that they provide a possibility to check the convergence of the simulated liquid-gas-solid systems into a state of equilibrium. We succeeded in showing that basic convergence is given, provided that adequate spatial resolutions are chosen. For the special problem of the floating stability of cuboid structures, convergence of numerical simulations towards the analytical model was obtained.

The idea of evaluating the simulated floating stability of rigid bodies was inspired by [14], who proposed it as a test case for a Navier-Stokes based simulator originally developed for the estimation of “green water” loads on ship decks [13]. As mentioned above, lattice Boltzmann based fluid-structure interaction techniques have been developed for the simulation of particulate flows. We were not able to find publications discussing the application of LBM-based free surface flows in interaction with floating structures. To our knowledge, the only approach to handle similar problems is the one proposed by Janßen [18].

2. Method

2.1. Isothermal D3Q19 Lattice BGK Method

We assume the *D3Q19* lattice model for 3-dimensional flows [31], with a set of $N = 19$ discrete *lattice velocities* c_i ($i = 0, \dots, N - 1$). For the theoretical considerations in this section, however, we will often fall back implicitly to the native *D2Q9* model, as it simplifies explanations and figures if they are 2-dimensional. The lattice velocities \vec{c}_i (also called *lattice directions* or *lattice links*) with their respective weights \vec{w}_i ($i = 0, \dots, N - 1$), as shown in Fig 1, are

$$\vec{c}_i = \begin{cases} (0, 0, 0) \\ (\pm 1, 0, 0), (0, \pm 1, 0), (0, 0, \pm 1) \\ (\pm 1, \pm 1, 0), (0, \pm 1, \pm 1), (\pm 1, 0, \pm 1). \end{cases} \quad (1)$$

In the following \bar{i} is used to denote the index of the lattice velocity $\vec{c}_{\bar{i}}$ with $\vec{c}_{\bar{i}} = -\vec{c}_i$.

Let s_x, s_y, s_z be positive real numbers divisible by the *spatial resolution*, constant δ_x . The domain $[0, s_x] \times [0, s_y] \times [0, s_z]$ is divided into *cells*, i.e., cubic volumes of length δ_x , which yields a computation domain of $\frac{s_x}{\delta_x} \times \frac{s_y}{\delta_x} \times \frac{s_z}{\delta_x}$ discrete lattice cells. Spatial quantities like s_x, s_y, s_z and δ_x are commonly given in a certain unit of length (e.g., metres). However – when dealing with LBM specific computations – dimensionless lattice coordinates are used: Spatial coordinates are thus given in the following as multiples of δ_x . By speaking of a cell (x, y, z) , where x, y and z are positive integer numbers we mean the lattice cell with respective volume $[x, x + 1] \times [y, y + 1] \times [z, z + 1]$ in the lattice. We refer to the point $(x + 0.5, y + 0.5, z + 0.5)$ as the *cell center*. For each lattice direction $i = 0, \dots, N - 1$ we name $f_i(\vec{x}, t)$ the *particle distribution function* (PDF) of the direction c_i in cell \vec{x} and of time step t .

The lattice BGK propagation scheme can be derived from the classic Boltzmann equation with the collision operator substituted by the *Bhatnagar Gross Krook* (BGK) operator [27]. Including an external force term F_i , the lattice BGK (LBGK) equation reads

$$f_i(\vec{x} + \delta_i \vec{c}_i, t + \delta_t) = f_i(\vec{x}, t) - \frac{1}{\tau} [f_i(\vec{x}, t) + f_{eq,i}(\rho(\vec{x}, t), \vec{u}(\vec{x}, t))] - \delta_t F_i. \quad (2)$$

τ is the dimensionless relaxation time and related to the *kinematic viscosity* ν by

$$\tau = \frac{\nu + 1/2c_s^2\delta_t}{c_s^2\delta_t}.$$

The lattice *speed of sound* c_s is a model-dependent constant. For the D3Q19 model it is $c_s = 1/\sqrt{3}$. The equilibrium function is therewith given as a so-called low Mach number expansion of the Maxwell distribution function [17],

$$f_{eq,i}(\rho, \vec{u}) = \rho w_i \left[1 + \frac{\vec{c}_i^T \vec{u}}{c_s^2} + \frac{(\vec{c}_i^T \vec{u})^2}{2c_s^4} - \frac{\vec{u}^T \vec{u}}{2c_s^2} \right], \quad (3)$$

and is valid only for small flow velocities, where the following constraint holds:

$$Ma := \frac{\vec{u}^T \vec{u}}{c_s^2} \ll 1. \quad (4)$$

The external force term F_i is used to represent gravitation (expressed as acceleration \vec{a}) in the simulation. It is given by [26]

$$F_i = w_i \rho \left(\frac{\vec{c}_i - \vec{u}}{c_s^2} + \frac{\vec{c}_i^T \vec{u}}{2c_s^4} \right) \vec{a}. \quad (5)$$

The local macroscopic quantities, density ρ and fluid momentum $\rho \vec{u}$, are obtained as moments from the PDFs:

$$\rho = \sum_{i=0}^{N-1} f_i, \quad (6)$$

$$\rho \vec{u} = \sum_{i=0}^{N-1} \vec{c}_i f_i. \quad (7)$$

$$\rho \vec{u} \vec{u}^T + p \mathbf{1} + S = \sum_{i=0}^{N-1} \vec{c}_i \vec{c}_i^T f_i \quad (8)$$

The last equation contains the momentum flux tensor $\rho \vec{u} \vec{u}^T$ and the stress tensor, where S represents the shear stresses of the flow. For a system in equilibrium, i.e. $f_i = f_{eq,i}$ ($i = 0..N - 1$), the stress tensor S vanishes.

Within this lattice Boltzmann model, the pressure is linearly related to the density, by the equation

$$p = c_s^2 \rho. \quad (9)$$

When a simulation includes an external force, e.g. in order to simulate the effect of gravity, stability concerns limit the density gradient and therefore the hydrostatic pressure gradient. Buick and Greated [7] give the following incompressibility condition which relates the external force \vec{a} to the projected height of the simulation domain in the force direction.

$$(l_x, l_y, l_z) \cdot \vec{a} \ll c_s^2. \quad (10)$$

$l_x = \frac{s_x}{\delta_x}$, $l_y = \frac{s_y}{\delta_y}$ and $l_z = \frac{s_z}{\delta_z}$ are the respective numbers of fluid cells in the x -, y - and z - direction.

In practice, the calculation according to the LBGK equation (2) is split up into two steps. First, a propagation step, the *stream step*, which propagates the local PDFs of each cell along the corresponding lattice link into the neighboring cell. The central one with zero lattice velocity remains on the same cell.

$$f'_i(\vec{x} + \vec{c}_i, t + 1) = f_i(\vec{x}, t) \quad (11)$$

Now, in the *collide step*, the relaxation towards the local equilibrium is performed for each cell with the set f'_i , $i = 0, \dots, N - 1$ of PDFs. The external force F_i is added. This yields the PDFs of the succeeding time step.

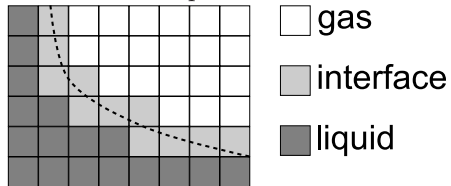
$$f_i(\vec{x}, t + 1) = f'_i(\vec{x}, t + 1) - \frac{1}{\tau} [f'_i(\vec{x}, t + 1) - f_{eq,i}(\rho, \vec{u})] - F_i. \quad (12)$$

For a step by step derivation of the lattice Boltzmann method see [16].

2.2. Previous Work: Free Surface LBM

The main characteristic of the free surface model given by [21] is that the dynamics of the second phase are neglected. It assumes a system of two immiscible fluids, in which the dynamics of the first phase govern the flow completely. We refer to this first phase as the *liquid* phase and to the second phase as the *gas* phase. The layer where the two phases come

Figure 2: 2D-Representation of a free liquid-gas boundary by interface cells. The real interface (dashed line) is captured by assigning the interface cells their liquid fraction.



in contact - the free surface - is assumed to be thin in relation to the spatial resolution δ_x . The separate regions of liquid or gas are on the other hand assumed to be large in comparison to δ_x . With this assumption, one can simulate the liquid phase by modeling the free surface as a special boundary condition. By means of a *volume of fluid* approach that introduces a dynamic *fill level* $\phi(\vec{x}, t)$ for each lattice cell, partial filling is allowed for cells at the free surface boundary. The fill level is the fraction of cell volume δ_x^3 that is currently filled with liquid, such that the liquid mass in a cell may be calculated as

$$m(\vec{x}, t) = \phi(\vec{x}, t) \cdot \rho(\vec{x}, t) \delta_x^3.$$

Cells that have a liquid fraction $\phi < 1$ and $\phi > 0$ thus form a boundary for the fluid referred to as the *interface*, and need special treatment, which is outlined in the following. We refer to those cells as *interface* cells. Fig. 2 shows the interface layer between liquid and gas for a virtual free surface, drawn as a dashed line. During the stream step, the fill level may change due to the exchange of PDFs with neighboring cells. The mass balance between two neighboring cells, \vec{x} and $\vec{x} + \vec{c}_i$, is given by

$$\Delta m_i = \begin{cases} 0 & \text{if } \vec{x} + \vec{c}_i \text{ is gas,} \\ f_i(\vec{x} + \vec{c}_i, t) - f_i(\vec{x}, t) & \text{if } \vec{x} + \vec{c}_i \text{ is liquid,} \\ \frac{1}{2}(\phi(\vec{x}, t) + \phi(\vec{x} + \vec{c}_i, t)) \cdot (f_i(\vec{x} + \vec{c}_i, t) - f_i(\vec{x}, t)) & \text{if } \vec{x} + \vec{c}_i \text{ is interface.} \end{cases} \quad (13)$$

The interface must further fulfill the characteristic of a free surface boundary. Because the gas flow is neglected in the model, only the pressure of the gas is taken into account at the interface between the two phases. Apart from that, the interface must freely follow the liquid flow, which is provided by a special *free surface boundary condition*. Assuming that an approximated normal vector $\vec{n}(\vec{x}, t)$ of the free surface is known for the interface cell at position \vec{x} , the PDFs f_i with $\vec{c}_i^T \vec{n} \leq 0$ (pointing towards the liquid phase) are set to

$$f'_i(\vec{x}, t + 1) = f_{eq,i}(\rho_G(\vec{x}), \vec{u}(\vec{x})) + f_{eq,\bar{i}}(\rho_G(\vec{x}), \vec{u}(\vec{x})) - f'_i(\vec{x}, t + 1) \quad (14)$$

during the stream step. Here $\rho_G(x)$ is chosen such that by Eq. 9 it matches the pressure p_G of the gas phase, which must be given. Indeed, Körner et al. [21] show that this results in a zero strain rate tensor for the boundary. This can be seen by substituting the reconstructed PDFs from Eq. 14 into the formula for the momentum flux and stress tensor, i.e., the second

order moment (Eq. 8) of the PDFs:

$$\begin{aligned}
\rho \vec{u} \vec{u}^T + p \mathbf{1} + S &= \sum_{i, \vec{c}_i^T \vec{n} > 0} \vec{c}_i \vec{c}_i^T f'_i(\vec{x}, t + 1) + \\
&\quad \sum_{i, \vec{c}_i^T \vec{n} \leq 0} \vec{c}_i \vec{c}_i^T [f_{eq,i}(\rho_G, \vec{u}) + f_{eq,\bar{i}}(\rho_G, \vec{u}) - f'_i(\vec{x}, t + 1)] \\
&= \sum_{i, \vec{c}_i^T \vec{n} \leq 0} \vec{c}_i \vec{c}_i^T [f_{eq,i}(\rho_G, \vec{u}) + f_{eq,\bar{i}}(\rho_G, \vec{u})] \\
&= \sum_{i=0}^{N-1} \vec{c}_i \vec{c}_i^T f_{eq,i}(\rho_G, \vec{u}).
\end{aligned}$$

Because the last sum resembles a system in equilibrium, it follows $S = \mathbf{0}$ and $p = c_s^2 \rho_G = p_G$.

The normal vector $\vec{n}(\vec{x})$ is obtained as approximation from the gradient of fill levels within a local neighborhood of the cell. It is also possible to include the effect of surface tension directly in the boundary condition above. If a constant surface tension parameter σ is given and the local curvature of the interface $\kappa(\vec{x}, t)$ is known, the gas pressure is augmented by the *Laplace pressure* to

$$p'_G = p_G + 2\sigma\kappa.$$

Pohl [30] proposed a method for 3D-calculations that include surface tension. His approach is, to extract the local curvature κ from the surface normals in a local neighborhood as a second step after the normal computation.

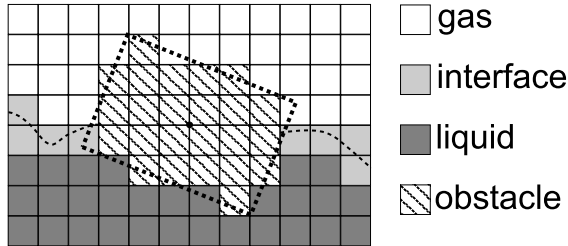
In order to allow free advection of the free boundary between gas and liquid, the state of the interface cells must be tracked carefully. Since the interface cells represent a boundary for the LBM scheme, it is necessary to assure a closed layer of interface cells around the liquid cells. This is facilitated by a set of *cell conversion rules*. Thus, no direct state transition between gas and liquid is allowed. If an interface cell reaches a fill level $\phi(\vec{x}) \leq -\epsilon$ or $\phi(\vec{x}) \geq 1 + \epsilon$ it is converted into a gas cell or a liquid cell, respectively. Since such a conversion could introduce holes in the interface, further cell conversions from either gas or liquid into interface cells may be triggered. The newly generated interface cells are initialized with a fill level $\phi = 0$ or $\phi = 1$, respectively. This cell conversion scheme has to be extended for the incorporation of floating objects, as shown in Sec. 2.4.

2.3. Previous Work: Particulate Flow LBM

Walls and other solid obstacles that block the fluid motion must be handled with appropriate boundary conditions. For this paper we assume that all solid boundaries can be modeled by a no-slip condition, i.e. the relative motion of the liquid at the boundary is zero. This can be achieved by reflecting distribution functions, that are hitting an obstacle cell during the stream step, to the opposed direction. If $f'_i(\vec{x})$ is given with an obstacle cell at $\vec{x} + \vec{c}_i$ it is bounced back according to

$$f'_i(\vec{x}, t + 1) = f_i(\vec{x}, t) + \frac{2}{c_s^2} w_i \vec{c}_i^T \vec{u}_w \rho, \quad (15)$$

Figure 3: A box-shaped rigid body mapped into the lattice. With a free surface flow, four different cell types have to be distinguished: Liquid, interface, gas and obstacle.



where \vec{u}_w is the velocity of the obstacle. The second term on the right hand side accelerates the fluid according to the movement of the wall [22]. If the solid is not moving ($\vec{u}_w = \vec{0}$), this term will vanish, and the boundary handling is reduced to a pure reflection.

From the boundary condition of Eq. 15 one can directly obtain the stresses exerted on the boundary. This is known as *momentum exchange* [22, 23, 28] in literature. The momentum transferred to the wall must equal the change of momentum which results from the reflection of the PDF, since elastic collisions are assumed. Thus, for a f_i reflected to f'_i by Eq. 15, the change in momentum is

$$\Delta \vec{j}_i = f'_i \vec{c}_i - f_i \vec{c}_i = 2\vec{c}_i (f_i + \frac{1}{c_s^2} w_i \vec{c}_i^T \vec{u}_w). \quad (16)$$

The simulation of immersed rigid bodies behaving according to Newtonian physics is facilitated by discretizing the shape of a body to the lattice. For every time step the no-slip boundary is set according to the object position and orientation. If the center of a cell is a point within the volume represented by the shape of the body, it is treated as an obstacle cell (Fig. 3). The movement of the rigid bodies resulting from the stresses, Eq. 16, including the resolution of body-body collisions, is realized in practice by coupling the lattice Boltzmann algorithm to a rigid body physics engine as in [20, 11]. The resulting body motion is then fed back to the fluid simulation by setting the boundary condition according to Eq. 15 in the cells covered by the obstacle. Hereby \vec{u}_w is given by the velocity of the body.

A given particle must behave according to the stresses exerted by the fluid. The net force and torque on the particle are obtained from the momentum flux according to Eq. 16, summed over the discretized particle surface. Let N_o be the set of grid points \vec{x} next to the discretized particle surface. For a cell $\vec{x} \in N_o$, let $I_o(\vec{x})$ be the set of indices $i \in I_o(\vec{x})$, where $\Delta \vec{j}_i(\vec{x})$ is defined due to a reflection of PDFs as stated above. Then the discrete surface integrals for force \vec{F}_{net} and torque \vec{T} , respectively, are given by

$$\vec{F}_{net} = \sum_{\vec{x} \in N_o} \sum_{i \in I_o(\vec{x})} \Delta \vec{j}_i(\vec{x}) \cdot \frac{\delta_x}{\delta_t}, \quad (17)$$

$$\vec{T} = \sum_{\vec{x} \in N_o} \sum_{i \in I_o(\vec{x})} (\vec{x} - \vec{o}) \times \Delta \vec{j}_i(\vec{x}) \cdot \frac{\delta_x}{\delta_t}. \quad (18)$$

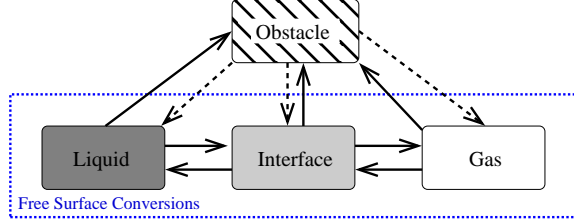


Figure 4: Allowed state transitions for cell types. With moving obstacles the number of transitions increases from four to ten. The free surface type conversions are framed by a dotted line. The dashed arrows indicate critical state changes from solid to fluid.

In the latter sum, \vec{o} is the center of gravity of the object. A non-zero torque acting on a freely moving rigid body will induce rotational movement of the body.

The momentum exchange method has become a kind of quasi-standard for the simulation of particle suspensions with Lattice Boltzmann and it has been mentioned in a large number of publications with only slight modifications. The main difference here to the works of Ladd [22, 23] or Aidun et al. [3, 4] is, that in our case the obstacle cells are always fluid blocking nodes. In the mentioned references there are “virtual” fluid nodes inside the discretized object shapes, which can be reactivated when uncovered by from the object. This approach, however, would be difficult to maintain in the presence of a liquid-gas flow, since it is unclear how the liquid-gas interface would have to be treated when intersecting with the volume of a particle.

2.4. A Liquid-Gas-Solid LBM

With the free surface model of Sec. 2.2 and the additional presence of moving obstacles from Sec 2.3, there are now two different boundaries for the liquid phase that must be treated dynamically. Fig. 3 illustrates the situation for a box floating on the free surface of a liquid, simulated according to Sec. 2.2. Since there are now four different types of cell states to consider (liquid, interface, gas, and solid) that may change according to fluid flow and object movement, the need for a sophisticated cell conversion algorithm arises. In the following, we show that these conversions can be organized in such a way that a consistent boundary around the liquid phase is assured in every time step.

Fig. 4 shows that the total number of conversions consists of ten state transitions. The transitions at the bottom are those of the advection scheme of the free surface model of Sec. 2.2 and need no further examination. The remaining transitions arise from the mapping of the solid to the grid. We assume the velocity of the object is small enough for conversions *into* obstacle to occur only at positions in the neighborhood of other obstacle cells; while conversions *from* obstacle to one of the three fluid states (liquid, interface or gas) can occur only at positions in the neighborhood of fluid cells. This is no additional limitation, but a direct consequence of the low Mach number limitation of the lattice Boltzmann scheme. Consider now an object penetrating the free surface as shown in Fig. 3. While conversions into obstacle cells are generally safe, the conversions from obstacle into fluid could lead to invalid lattice configurations with holes in the interface layer. Thus the correct cell type, i.e., liquid, interface or gas, needs to be determined such that a valid lattice configuration

is adhered for the next time step. This is achieved by an update rule based on the local neighborhood of a given obstacle cell.

We define the non-obstacle neighborhood of a cell as $B(\vec{x}) := \{\vec{x} + \vec{c}_i \mid \vec{x} + \vec{c}_i \text{ is no obstacle}\}$. For a prior obstacle cell \vec{x} to be converted into fluid, the state is determined as follows [5].

- $B(\vec{x})$ contains no liquid: \vec{x} is converted into gas.
- $B(\vec{x})$ contains no gas: \vec{x} is converted to liquid, $\rho(\vec{x})$ is interpolated from $B(\vec{x})$, and the $f_i(\vec{x})$ are set to $f_{eq,i}(\rho(\vec{x}), \vec{u}_w)$, where \vec{u}_w is the velocity of the point on the object's surface, which is closest to the cell center of \vec{x} .
- $B(\vec{x})$ contains liquid and gas: \vec{x} is converted into interface. $\rho(\vec{x})$ is interpolated from the non-gas cells in $B(\vec{x})$, and the $f_i(\vec{x})$ are set as in the preceding case. Additionally a fill level $\phi(x)$ is chosen by interpolation of the fill levels of the interface cells in $B(\vec{x})$. It is also possible to include the gas cells with the pressure ρ_G in the interpolation of ρ , since pressure can be seen as a continuous quantity across the free surface boundary of Eq. 14.

With the free surface model of Sec. 2.2, the gas phase is only taken into account in terms of a pressure force exerted onto the free surface. This pressure forces, however, are also acting on the surface of the solid bodies. So, in analogy to the boundary condition for the free surface, Eq. 14, we use the equilibrium function, Eq. 3, to construct PDFs $f_{eq,i}(\rho_G, \vec{0})$ for the lattice links from gas, or interface cells to the obstacle cell of an object. From these the momentum transferred to the body can be calculated from Eq. 16. The value of the constructed PDF is linearly interpolated with the liquid's distribution function f_i . Thus, in presence of gas in the neighborhood of an obstacle cell, the momentum acting on the body locally is given by

$$\Delta \vec{j}_i = 2\vec{c}_i \left(\phi \cdot f_i + (1 - \phi) \cdot f_{eq,i}(\rho_G, \vec{0}) + \frac{\phi}{c_s^2} w_i \vec{c}_i^T \vec{u}_w \right). \quad (19)$$

For a gas cell, $\phi = 0$, only the equilibrium function of Eq. 16 remains, all other parts vanish.

3. Simulation of Floating Bodies

In the following sections we present the results of calculations performed with the method of Sec. 2.4, i.e., various simulations of a rigid body exposed to a free surface flow. Since many details of the method are owed to previous particulate flow simulations, we briefly recapitulate the most relevant results in Sec. 3.1. We then focus on the evaluation of forces and motion of partially immersed rigid bodies, Sec. 3.2, in order to prove the basic consistency of the method. When dealing with floating objects in gravity-stratified free surface flows, the buoyancy forces on the discretized objects turned out to be one of the main sources of error. In the last part, Sec. 3.3, we apply our method to the problem of floating stability of rigid bodies.

3.1. Force Computations with Spherical Particles and Staircase Approximation

It has to be emphasized that due to the discretization of the body shapes to lattice sites as described in the previous section, a certain *a priori* error is introduced. This is a well-known issue in LBM-based particulate flows, and there has been a lot of research regarding the treatment of complex, curved boundaries in lattice Boltzmann over the last decades [31, 2]. These schemes allow second order spatial accuracy in the treatment of curved boundaries. Most of them are directly applicable for moving boundaries, such as particles. However, in the kind of flows which we are going to discuss in the final part of the paper, interpolation based schemes like [6], or [35], which have been applied with success to particle simulations in the past, turned out to be little useful.

The solid particle model described in Sec. 2.3 which we use throughout this paper is identical to the one used for drag force computations on suspended particle agglomerates in [11, 20], where the net force deviation was studied with spherical particles in stokes flow. The calculations were performed with various degrees of spatial resolution and a set of different lattice relaxation parameters τ in [11] with a sphere fixed to the center of a channel flow. The results were found to be in good agreement with theoretical expectations. Second order boundary conditions surpassed the staircase approximation under all tested circumstances. In [20], sinking sphere simulations were conducted in order to evaluate the method with moving particles as proposed in [1]. These simulations included the influence of gravity, and used the unified boundary treatment by [35] for the solid boundaries: A particle of density $\rho_s > 1$ accelerates until the frictional force imposed by the fluid surrounding balances its weight and a terminal sinking velocity is reached. The results showed small periodic oscillations in the measured force on a sphere that moves with a quasi-constant velocity through the lattice. This error can be attributed to the staircase approximation of the boundary of the body. Fig. 5 shows the volume error for a sphere of radius $5 \delta_x$ when traveling along an axis-aligned path. The number of cells actually covered by the sphere is depending on its exact position relative to the lattice. With the discretized shape of a particle changing, the set of lattice links included in the discrete surface integral around its boundary changes and so does the net force, Eq. 17, and torque, Eq. 18, respectively. The interpolation based schemes applied in [11, 20] however, approximate a curved boundary by calculating its exact distance from the cell center along the lattice link of reflection. This information is used to correct the reflected PDFs from Eq. 15. Hence, the error arising in the buoyancy force from changes in the discrete volume of an object cannot be corrected by purely local refinements. For liquid-solid suspensions without a free surface the problem of buoyancy force fluctuations with fluid-blocking obstacles is usually negligible, or can be corrected by workarounds as reported in [15]. The following subsections discuss this issue for the free surface case.

3.2. Forces on Buoyant Rigid Bodies

Due to the staircase approximation of rigid body shapes, not only is the buoyancy force depending on the object's position, but – for partially immersed objects – a staircase function with respect to draft. This can be best explained for an axis-aligned cube of side length s

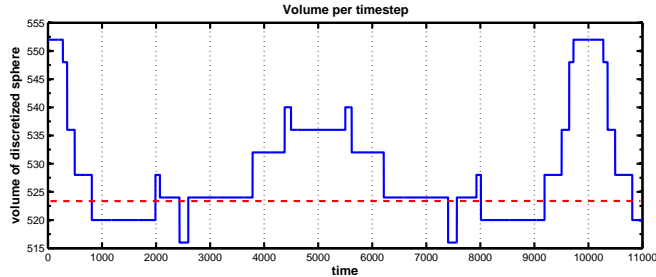


Figure 5: Discretized volume for a spherical particle traveling along an axis-aligned path with a velocity of 10^{-4} . Ideal volume: 523.6. The graph repeats periodically every 10000 time steps

in a liquid at rest with a constant water level. The buoyant force is then given as a linear function with respect to the draft d :

$$F_B = \rho g s^2 d.$$

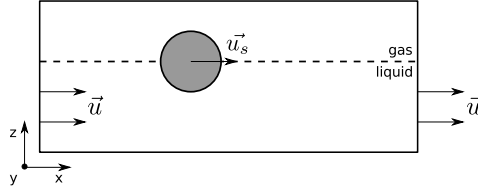
Because of the discretization error, d is only exact up to the lattice resolution δ_x . This can keep buoyant objects from coming to rest at their equilibrium position. Especially for objects with lattice-aligned planar faces such as a cube this would sometimes cause an unphysical “wobbling” behavior with the object jumping between two points slightly below and above the ideal floating position. If on the contrary a fixed cuboid is considered and the gauge of the liquid is varied immersing more or less of the object’s surface, the changes in the buoyant force on the object would be continuous. This is because the volume of fluid-based interface treatment is not limited to the spatial accuracy of the lattice. The fill level is taken into account in the force calculations in the interface cells at the triple line of liquid, gas and solid by Eq. 19. Test cases with a linearly rising water level around a partially immersed, axis-aligned, fixed cuboid led to a linear increase in the buoyant force.

3.2.1. Free Advection Test

To test the consistency of the unified liquid-gas-solid algorithm, a *free advection test* was performed in a channel flow with a constant homogeneous velocity in the laminar regime along the x-direction, and a gravitational field along the z-axis. A spherical particle of density $\rho_s = 0.5$ was placed freely floating in the center of the channel to be accelerated by the hydrodynamic forces acting on its surface. Fig. 6 gives an impression of the simulated setup. Because the gas phase is neglected in the model it must not hinder the particle motion in any way. This means, that in both cases the final velocity of the particle must equal the fluid velocity. After the systematic drag force evaluation cited in the preceding section, this test might seem trivial at the first spot. But in the presence of a density gradient and because of the changes in the discretized particle shape (Sec. 3.1), there are at least two important sources of error to consider. Hence, in the following we also examine the results at critical flow velocities that have the same order of magnitude as the expected errors.

The channel size measured $60 \times 40 \times 30$ lattice units, and the particle diameter was $12\delta_x$. All long sides of the channel were no-slip moving walls (Eq. 15), in order to obtain a homogeneous velocity profile across the domain with a constant flow velocity u along the

Figure 6: Schematic view for a free advection test with a floating sphere in laminar free surface flow. The channel is driven by a moving wall boundary condition at the bottom and its longitudinal side planes. The channel entry and outflow are connected with each other by means of a periodic boundary condition.



x-axis. The left ($x = 0$) - and right ($x = s_x$) - boundaries were connected periodically, by copying PDFs streamed outside at one end into the cells at the opposing end of the domain.

The whole process of testing was performed at four different values of $\tau_{1..4}$, namely 0.62, 0.8, 1.1, 1.7 a gravitational constant of $g = 10^{-5}$, and four different channel velocities $u_{1..4} = 10^{-4}, 5 \cdot 10^{-5}, 2.5 \cdot 10^{-5}, 1 \cdot 10^{-5}$. In order to check for possible sources of errors the scenario was run in a sequence of increasing complexity, starting with a simplified version of the simulation experiment. The first series were the following.

- Channel fully filled with liquid without gas; without gravitational field.
- Repetition without gas, but with gravitational field as stated above. The particle density was set to 1.0 in this case.

In the first run the particle velocity matched the liquid velocity to the last digit without any deviations. For the second run we were expecting errors due to oscillations in the buoyant force as described above. These were clearly measurable, and largest for the lowest lattice viscosity $\tau_1 = 0.62$, where the z-component of the object velocity oscillated within the interval $[-g, +g]$. For larger τ values the effect would be damped (e.g., by a factor of 0.1 in the case of τ_4). There were no significant deviations in the other velocity components of the particle.

The next test series consisted of the channel partially filled with liquid with a planar free surface at $z = 19.5$ under the influence of gravity. The particle was removed to check the behavior of the interface cells. The free surface remained planar under all tested circumstances, as expected. For the lowest value of $\tau = 0.62$, locally spurious interface velocities were occurring. However, the absolute deviation from the bulk viscosity was always below 10^{-5} , restricted locally to parts of the interfacial layer, and therewith only critical for low velocities.

We finally tested the advection of a solid body in the free surface flow by placing the particle with density $\rho_s = 0.5$ inside the channel. The fluctuations in the lifting force were comparable to those measured in the all-liquid domain under gravity with all tested cases. However, here the error also became visible in the in the other components of the net force on the object, and thus introduced an error in the streaming velocity of the particle. We believe that this is caused by the errors introduced by the refilling step of the algorithm, when obstacle-to-fluid conversions occur for an object sticking through the interface layer. As described in Sec. 2.4, we initialize these cells to a local equilibrium with parameters interpolated from a local neighborhood. This is likely to introduce a certain error that cannot

be balanced in the asymmetrical case when an obstacle is at the boundary between gas and liquid. Even in case of liquid-solid flows without a gas phase, the problem of initializing new liquid cells is non-trivial [8].

We have not evaluated those cases, where the empty channel showed spurious currents. These were: $\tau_1 = 0.62$ with velocities u_2, \dots, u_3 . In the remaining cases the sphere would follow the current with the velocities given in Tab. 1. For higher flow velocities (or lower values of g), this error would no longer be critical, if even apparent in the sphere velocities.

Table 1: Errors in the velocity of the sphere for lattice gravity of $g = 10^{-5}$: Critical if τ is low and the characteristic flow velocity of the same order as g .

τ	u_1	u_2	u_3	u_4
0.62	1.1e-4	n.e.	n.e.	n.e.
0.8	1.05e-4	5.5e-5	3.0e-5	2.0e-5
1.1	1.01e-4	5.15e-5	2.8e-5	1.3e-5
1.7	1.e-4	5.05e-5	2.55e-5	1.1e-5

The the systematic error in the staircase approximated objects is negligible as long as the characteristic velocity U of the flow is large in comparison with the gravitational constant. However, it should be considered in the Froude number scaling [19] ($Fr = U/\sqrt{gL}$, for a characteristic length L) of simulations. On the other hand the question arises, whether a more accurate treatment of particle boundaries can be achieved that does not suffer from the presence of a hydrostatic density gradient. We were unable to find any literature that reports the problem explicitly. Besides increasing the spatial resolution, or applying local grid refinement methods that entail complex restructuring of the whole implementation of the method, we found at least one approach that could provide a significant improvement. Based originally on Chen et al., a volumetric interpretation [9] of the lattice Boltzmann method allows the direct calculation of the momentum flux onto finite surface elements. This can be exploited to realize boundary conditions, like [10, 34, 32], that offer sub-grid scale accuracy. [32] presented a variant that allows an exact description of the surface of obstacles including surface stress calculation which is independent of surface motion. As the free surface boundary treatment, Eq 14, is in principle also a volumetric approach [21], this would yield a further unification of the method described in this paper. We expect to explore this issue in future publications.

3.3. Stability of Floating Bodies

We now apply the method on the problem of floating stability of non-spherical rigid bodies. Archimedean law appears to be quite intuitive, which states that the buoyancy experienced by an immersed object is equal to the weight of the liquid displaced by ∇ , the immersed volume part of the body (i.e., the part below the water plane). According to that rule, a body with a specific material density $\rho_s < 1.0$ will sink down or rise up until buoyant force $\vec{F}_B = \rho g \nabla$ and gravitational force \vec{F}_G balance each other vertically. In practice, however, even if this balance of forces is given, the resulting equilibrium is often found to be unstable. Consider for instance a cube in 2-D as shown in Fig. 7. In both positions exactly

Figure 7: For both positions of the cube of specific density $\rho_s = 1/2$ hydrostatic equilibrium is given. However the equilibrium on the left hand side is unstable. A stable equilibrium can be found with the cube rotated 45 degrees.

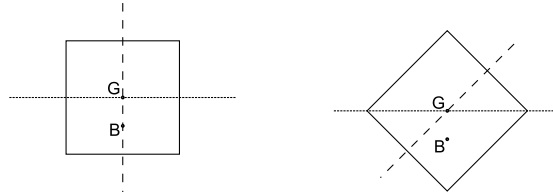


Figure 8: Stable floating positions for a cube of material density $\rho_s = 1/4$ (left) and $\rho_s = 3/4$ (right), respectively. Each time one corner of the cube is in place with the water line while another one is exactly half-immersed.

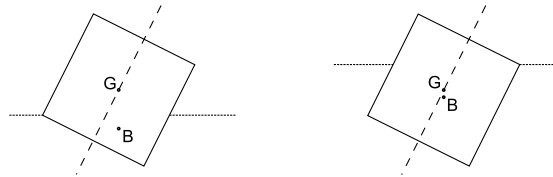


Figure 9: Unstable equilibrium of a cube. Because of the slight horizontal displacement of the center of buoyancy B relative to the center of gravity of the cube G , a moment occurs that pushes the cube further from its upright position. The center of buoyancy B is constructed as the center of gravity of the trapezoid, which the immersed part of the cube makes up together with the fluid surface. To construct B , the base line segment u is elongated in one direction by the parallel opposite segment v , while the latter is again elongated in the opposite direction by base line u . Next, the shifted end points of each line segment are connected. The intersection of the connecting line with the line through the midpoints of u and v gives its center of gravity of the trapezoid, B .

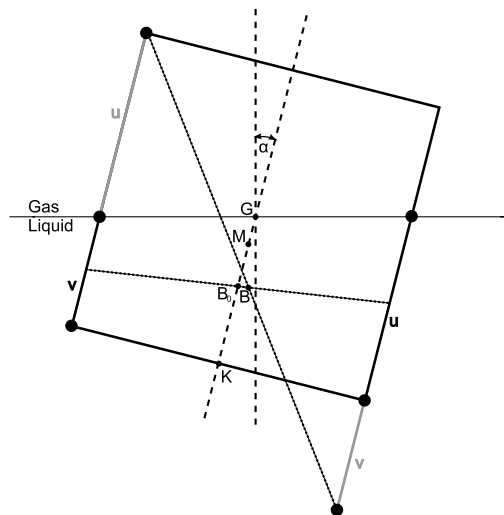
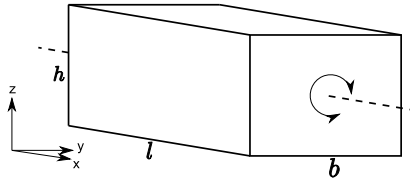


Figure 10: Box rotating about its longitudinal axis (rolling motion).



half of the body volume is immersed and thus the body floats in hydrostatic equilibrium. However, it can be shown that only the right hand side with an heel angle of 45 degrees is stable. To see this, consider the cube slightly rotated from its upright position, such that its central axis (dashed line in Fig. 7) is heeled by a small angle α . The *center of gravity* G of the cube is the point on which the gravitational force \vec{F}_G acts vertically downward. The *center of buoyancy* B , which is defined as the center of gravity of the immersed part ∇ of the body, is slightly displaced to the left as shown in Fig 9. Thus with \vec{F}_B acting on B vertically upward, a rotational moment in the heeling direction occurs, pushing the cube further from its upright position. In the same way it can be shown that, starting from the 45 degree rotated position (right in Fig 7), small angles of heel from this position lead to a righting moment in the opposite direction. The result is a stable equilibrium at this position. Fig. 8 shows two more stable floating positions for the cube densities $\rho_s = 1/4$ and $\rho_s = 3/4$.

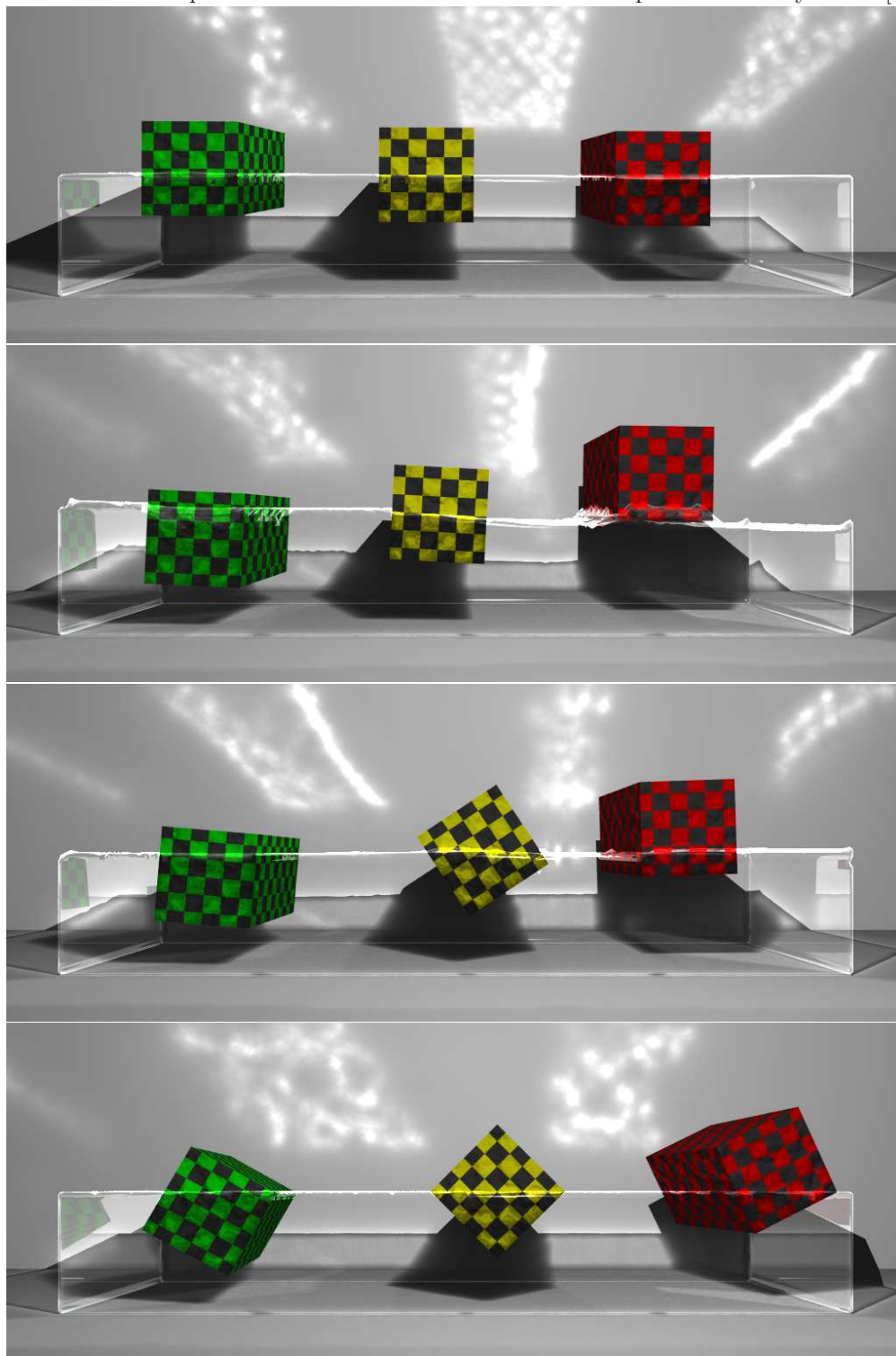
3.3.1. Equilibrium Position of Floating Cubes

Following [14], we check the rotational equilibrium of floating cubes of density $\rho_s = 0.25$, 0.5, and 0.75 in simulations. With the given densities 0.25 and 0.75 a stable angle of heel is found at 26.565° from the upright axis of the cube as shown in Fig. 8. The cube of density 0.5 should calibrate to 45° . Since we are dealing with 3-dimensional objects, the 2D cube of side length s is represented by a cuboid of dimensions $2s \times s \times s$, that will rotate around its longitudinal axis only, as in the schematic of Fig. 10. Inside a domain of $130 \times 40 \times 40$ cells, the lower half was filled liquid with lattice viscosity $\tau = 1/1.9 = 0.526$ and initialized with hydrostatic pressure ($g = 7.5 \cdot 10^{-4}$). Three boxes with $s = 16$ were placed inside the basin, slightly heeled from their axis-aligned upright position by an angle of 2.86° . The simulation was run until all fluid motions ceased and the objects came to rest. Fig. 11 shows visualizations of the simulated scenario at various time steps. Since the initial positions of the objects were far from the equilibrium state, their motions would cause a wavy disturbance of the liquid in the basin. It can be clearly seen from these visualizations that even at this low resolution a strong convergence towards the ideal equilibrium was given.

3.3.2. Righting Stability Moment of Wall-Sided Structures

Consider again a floating structure heeled about a certain angle α about its upright axis. The intersection of the line with direction \vec{F}_B through B with the upright axis of a body is defined as the *metacenter* M . If M lies above the center of gravity G then the floating position of the body will be stable, otherwise unstable (see Fig. 9). This concept originates from marine engineering and is commonly used in the characterization the floating stability of ships and other offshore structures. A comprehensive discussion can be found in [19]. The

Figure 11: Box objects of density 0.75, 0.5 and 0.25, respectively, striving towards vertical and rotational equilibrium. The first three pictures show the system in motion. The last picture was taken after all visible motions had ceased. All snapshots were visualized from simulation output with the ray tracer [29].



lever arm of the torque arising from the horizontal displacement of the mass centers B and G is given by $\overline{GM} \sin \alpha$, and hence the *righting stability moment* of the body can be calculated as

$$m_s = \vec{F}_B \cdot \overline{GM} \sin \alpha.$$

The curve $m_s(\alpha) = \vec{F}_B \cdot \overline{GM} \sin \alpha$ is called the *stability curve* of the floating object. This curve can be derived analytically for many relevant situations, depending on the shape of the immersed structure. An important case is that of a *wall-sided* structure, where the points of the structure's surface sinking under or rising above the water plane upon the considered angles of heel are parallel opposing sides when the structure is upright. If a wall-sided structure is given, then, according to [19, 12], the Scribanti formula states

$$\overline{B_0M} = \frac{I}{\nabla} \cdot \left(1 + \frac{1}{2} \tan^2 \alpha\right),$$

where B_0 is the center of buoyancy of the upright position, I is the moment of inertia of the water plane and ∇ stands for the immersed volume of the whole body. In case of a cuboid of length l , width b , height h and draft d ($= \rho_s \cdot h$ – obtained from the non-heeled position), the formula can be simplified by putting

$$\frac{I}{\nabla} = \frac{1}{12} \frac{b^2}{d},$$

and with K as the keel point of the cuboid, an expression for \overline{GM} can be introduced as

$$\overline{GM} = \overline{KB_0} + \overline{B_0M} - \overline{KG}.$$

From this, the ideal stability curve of an arbitrary cuboid can be calculated. Fig. 12 shows the schematic stability curves for some cuboid structures of density $\rho_s = 1/2$ and various width:height ratio. In case of a cube, the stability curve has a negative slope at the origin. This shows, that the upright position is an unstable equilibrium. Increased width yields a higher floating stability.

To further test the force calculation on floating bodies, the righting stability moment of a floating cube at different angles of heel was measured in lattice Boltzmann simulations and compared to the ideal stability curve of the structure. In all of the following cases, the gravitational constant was chosen to be $g = 10^{-4}$ and a partially filled basin was initialized with a pressure gradient according to hydrostatic equilibrium. The relaxation time was $\tau = 1.0$. The initial width to height ratio of the box was 6 : 4 (a), and then in a second pass a lower ratio of 5 : 4 (b) was chosen. Each time, the error was examined at three different resolutions, i.e., the box size ($b \times h$) in lattice units was 24×16 , 48×32 , 96×64 and 20×16 , 40×32 , 80×64 , respectively. The length side along the axis of rotation was always chosen as $l = 2h$. The box was positioned axis-aligned with the lattice, exactly half-immersed relative to the free surface plane. During the simulation, the box was fixed to a constant position and the angle of heel of the half-immersed box was varied with α in $0^\circ..30^\circ$ around the longitudinal axis of the box through its center of gravity.

Figure 12: Stability curves for various floating cuboids of density $1/2$. From the negative slope of the graph for the cube case (width:height ratio 4 : 4) at 0° angle of heel, it can be deduced that the upright position is unstable. The stability increases if the width is enlarged.

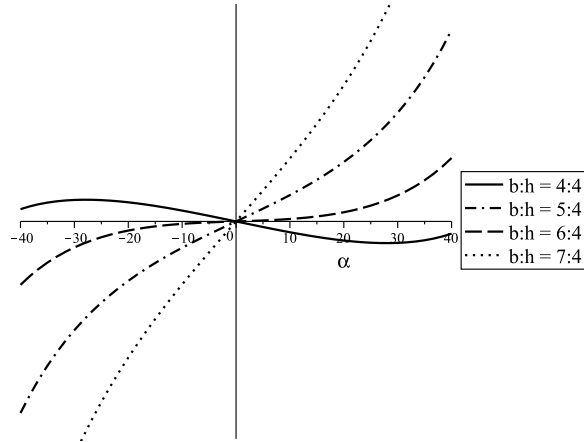


Figure 13: Stability curve of a heeled cuboid at different resolutions $dx = 1, 0.5, 0.25$. The legend reads the width of the box in lattice units at the different resolutions. There are significantly less deviations in the torque of the more stable box of width per height ratio 6:3 (a) compared to the box shape of ratio 5:4 (b).

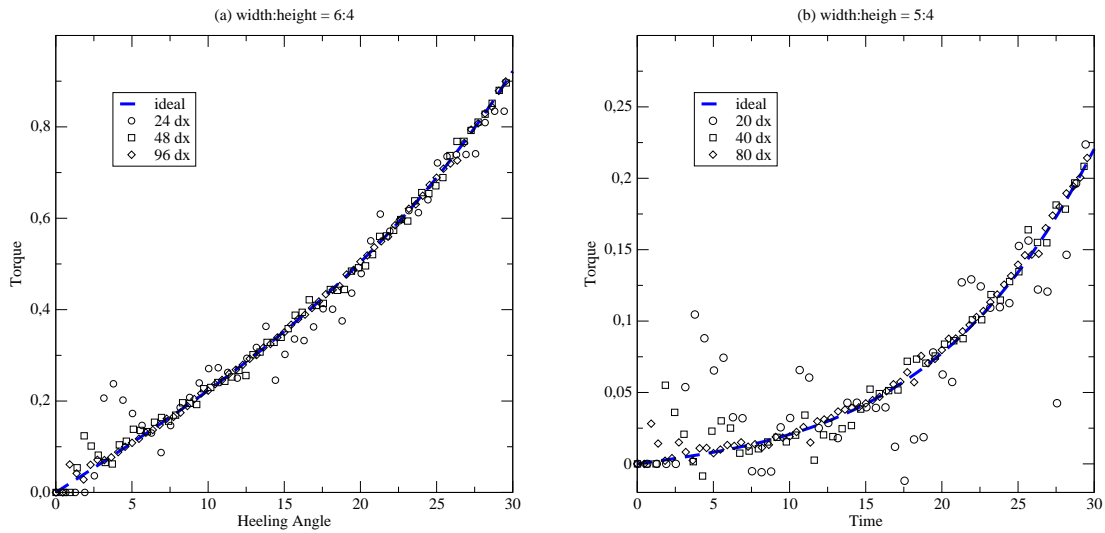


Fig. 13 shows the simulation results compared to the ideal stability curve. The error was much larger in the second case (b), since the stability lever arm of the box is shorter at the lower width per height ratio. Thus even small errors in the box discretization have a visible influence on the behavior of the box. However, in all cases it can be seen that the errors are decreasing at higher resolutions. Convergence towards the ideal values was clearly given.

4. Conclusion

In this paper we described a method for the simulation of liquid-gas-solid flows by means of the lattice Boltzmann method. Based on previous works, the momentum exchange method is used to obtain fluid stresses at the surface of rigid bodies, which allows to calculate the resulting net force and torque. A novel set of cell conversion rules (Sec. 2.4) allows unrestricted movement of the solid bodies within the domain, including penetrations of the free surface. We demonstrated the consistency of the method in a free advection test with a particle following a homogeneous free surface channel flow under the influence of gravity in Sec. 3.2.

For further validation of force and torque calculations on non-spherical rigid bodies, we applied the method to the classic mechanical problem of floating stability of immersed structures. Basic convergence towards the equilibrium state was successfully checked for the case of box objects with square sides. We took advantage of the fundamental stability formulae for wall-sided structures and validated the righting moment of box shaped objects under varying angles heel. The results were found to converge towards the ideal values with increased spatial resolution.

As a next step it would be interesting to move on from these hydrostatic stability examples towards dynamic ones, that include coupled interaction of liquid and solid objects. We will present further results together with method improvements in future publications.

5. Acknowledgements

For the simulations presented in this paper, the *waLBerla* lattice Boltzmann framework [25] and the *pe* rigid body physics engine [24] have been used. These software projects are a collaborative effort of the Chair for System Simulation at the University of Erlangen-Nürnberg.

The author would like to thank Jan Götz, Dr. Klaus Iglberger, Daniela Anderl, Dr. Stefan Donath, Matthias Markl, Tobias Preclik and Florian Schornbaum for various discussions and corrections. Finally, many thanks go to Dr. Christian Janßen for his kind correspondence via electronic mail.

References

- [1] C. K. Aidun, Y. Lu, and E.-J. Ding. Direct analysis of particulate suspensions with inertia using the discrete boltzmann equation. *J. Fluid Mech*, 373, 1998.

- [2] Cyrus K. Aidun and Jonathan R. Clausen. Lattice-boltzmann method for complex flows. *Annu. Rev. Fluid Mech.*, 42, 2010.
- [3] Cyrus K. Aidun and Yannan Lu. Lattice boltzmann simulation of solid particles suspended in fluid. *Journal of Statistical Physics*, 81 (1/2), 1995.
- [4] Cyrus K. Aidun and Yannan Lu. Extension of the lbm for direct simulation of suspended particles near contact. *Journal of Statistical Physics*, 112 (3/4), 2003.
- [5] S. Bogner. Simulation of floating objects in free-surface flows. Master's thesis, University of Erlangen-Nuremberg, Lehrstuhl für Informatik 10 (Systemsimulation), Institut für Informatik, 2009.
- [6] M. Bouzidi, M. Firdaouss, and P. Lallemand. Momentum transfer of a boltzmann-lattice fluid with boundaries. *Physics of Fluids*, 13(11), 2001.
- [7] J.M. Buick and C.A. Greated. Gravity in a lattice boltzmann model. *Phys. Rev. E*, 61(5), 2000.
- [8] A. Caiazzo. Analysis of lattice boltzmann nodes initialization in moving boundary problems. *Progress in Computational Fluid Dynamics*, 8 (1-4):3, 2008.
- [9] Hudong Chen. Volumetric formulation of the lattice boltzmann method for fluid dynamics: Basic concept. *Physical Review E*, 58(3), 1998.
- [10] Hudong Chen, Chris Teixeira, and Kim Molvig. Realization of fluid boundary conditions via discrete boltzmann dynamics. *International Journal of Modern Physics C*, 9(8), 1998.
- [11] Binder Christian, Feichtinger Christian, Schmid Hans-Joachim, Thürey Nils, Peukert Wolfgang, and Rüde Ulrich. Simulation of the hydrodynamic drag of aggregated particles. *Journal of Colloid and Interface Science*, 301, 2006.
- [12] Captain D.R. Derrett and C.B. Barrass. *Ship Stability for Masters and Mates*. Butterworth-Heinemann, 1999 (1964). 5th edition.
- [13] G. Fekken, A.E.P. Veldman, and B. Buchner. Simulation of green water loading using the navier-stokes equations. In J. Piquet, editor, *Proceedings 7th International Conference on Numerical Ship Hydrodynamics*, 1999.
- [14] Geert Fekken. *Numerical Simulation of Free-Surface Flow with Moving Rigid Bodies*. PhD thesis, Rijksuniversiteit Groningen, 2004.
- [15] Jan Goetz. *Massively Parallel Direct Numerical Simulation of Particulate Flows*. PhD thesis, University of Erlangen-Nuremberg, 2011.
- [16] Dieter Hänel. *Molekulare Gasdynamik*. Springer, 2004. german.

- [17] X. He and L.-S. Luo. Theory of the lattice boltzmann method: From the boltzmann equation to the lattice boltzmann equation. *Phys. Rev. E*, 56(6), 1997.
- [18] Christian Janßen. *Kinetic approaches for the simulation of non-linear free surface flow problems in civil and environmental engineering*. PhD thesis, Technische Universität Braunschweig, 2010.
- [19] J.M.J. Journée and W.W. Massie. *Offshore Hydromechanics*. Delft University of Technology, 2001. <http://www.shipmotions.nl>.
- [20] Iglberger Klaus, Thürey Nils, and Rüde Ulrich. Simulation of moving particles in 3d with the lattice boltzmann method. *Computers and Mathematics with Applications*, 55 (7), 2008.
- [21] C. Körner, M. Thies, T. Hofmann, N. Thürey, and U. Rüde. Lattice boltzmann model for free surface flow for modeling foaming. *Journal of Statistical Physics*, 121 (1/2), 2005.
- [22] A.J.C. Ladd. Numerical simulations of particulate suspensions via a discretized boltzmann equation part i. theoretical foundation. Lawrence Livermore National Laboratory, 1993.
- [23] A.J.C. Ladd. Numerical simulations of particulate suspensions via a discretized boltzmann equation part ii. numerical results. Lawrence Livermore National Laboratory, 2007.
- [24] University of Erlangen-Nuremberg Lehrstuhl für Informatik 10. pe - rigid body physics engine, 2005-2011. URL <http://www10.informatik.uni-erlangen.de/Research/Projects/pe/>.
- [25] University of Erlangen-Nuremberg Lehrstuhl für Informatik 10. walberla - lattice boltzmann framework, 2006-2011. URL <http://www10.informatik.uni-erlangen.de/de/Research/Projects/walberla/>.
- [26] L.-S. Luo. Unified theory of lattice boltzmann models for nonideal gases. *Phys. Rev. Lett.*, 81(8), 1998.
- [27] L.-S. Luo. Theory of the lattice boltzmann method: Lattice boltzmann models for nonideal gases. *Phys. Rev. E*, 62(4), 2000.
- [28] R. Mei, D. Yu, W. Shyy, and L.-S. Luo. Force evaluation in the lattice boltzmann method involving curved geometry. *Physical Review E.*, 65, 2002.
- [29] Persistence of Vision Pty. Ltd. Persistence of vision (tm) raytracer, 2004. <http://www.povray.org>.
- [30] T. Pohl. *High Performance Simulation of Free Surface Flows Using the Lattice Boltzmann Method*. PhD thesis, University of Erlangen-Nuremberg, 2007.

- [31] Mei R., Shyy W., Yu D., and Luo L-S. Lattice boltzmann method for 3-d flows with curved boundary. *Journal of Computational Physics*, 161, 2000.
- [32] M. Rhode, J.J. Derksen, and H.E.A. Van den Akker. Volumetric method for calculating the flow around moving objects in lattice-boltzmann schemes. *Physical Review E.*, 65, 2002.
- [33] Sauro Succi. *The Lattice Boltzmann Equation for Fluid Dynamics and Beyond*. Oxford Science Publications, 2001.
- [34] R. Verberg and A.J.C. Ladd. Lattice-boltzmann model with sub-grid-scale boundary conditions. *Physical Review Letters*, 84(10):2148, 2000.
- [35] D. Yu, R. Mei, and W. Shyy. A unified boundary treatment in lattice boltzmann. In *41st Aerospace Sciences Meeting & Exhibit*. American Institute of Aeronautics and Astronautics, Inc., 2003.